

University of Groningen

Charge and spin transport in two-dimensional materials and their heterostructures

Bettadahalli Nandishaiah, Madhushankar

DOI:
[10.33612/diss.135800814](https://doi.org/10.33612/diss.135800814)

IMPORTANT NOTE: You are advised to consult the publisher's version (publisher's PDF) if you wish to cite from it. Please check the document version below.

Document Version
Publisher's PDF, also known as Version of record

Publication date:
2020

[Link to publication in University of Groningen/UMCG research database](#)

Citation for published version (APA):

Bettadahalli Nandishaiah, M. (2020). *Charge and spin transport in two-dimensional materials and their heterostructures*. [Thesis fully internal (DIV), University of Groningen]. University of Groningen.
<https://doi.org/10.33612/diss.135800814>

Copyright

Other than for strictly personal use, it is not permitted to download or to forward/distribute the text or part of it without the consent of the author(s) and/or copyright holder(s), unless the work is under an open content license (like Creative Commons).

The publication may also be distributed here under the terms of Article 25fa of the Dutch Copyright Act, indicated by the "Taverne" license. More information can be found on the University of Groningen website: <https://www.rug.nl/library/open-access/self-archiving-pure/taverne-amendment>.

Take-down policy

If you believe that this document breaches copyright please contact us providing details, and we will remove access to the work immediately and investigate your claim.

Downloaded from the University of Groningen/UMCG research database (Pure): <http://www.rug.nl/research/portal>. For technical reasons the number of authors shown on this cover page is limited to 10 maximum.

5 Electronic properties of germanane field-effect transistors

Abstract

A new two dimensional (2D) material - germanane has been synthesized recently with promising electrical and optical properties. In this chapter, we report the first realisation of germanane field-effect transistors fabricated from multilayer single crystal flakes. Our germanane devices show transport in both electron and hole doped regimes with ON-OFF current ratio of up to 10^5 (10^4) and carrier mobilities of $150 \text{ cm}^2\text{V}^{-1}\text{s}^{-1}$ ($70 \text{ cm}^2\text{V}^{-1}\text{s}^{-1}$) at 77 K (room temperature). A significant enhancement of the device conductivity under illumination with 650 nm red laser is observed. Our results reveal ambipolar transport properties of germanane with great potential for (opto)electronics applications.

Published as:

B.N. Madhushankar, A. Kaverzin, T. Giousis, G. Potsi, D. Gournis, P. Rudolf, G.R. Blake, C.H. van der Wal, B.J. van Wees,

2D Materials 4 (2), 021009 (2017).

5.1 Introduction

The exceptional transport properties of graphene have generated an immense impulse that has stimulated the scientific community to study other layered Van der Waals materials¹⁻³. Graphene analogues such as germanene, silicene, and stanene, as a separate family with hexagonal crystal structures, deserve careful consideration as they promise high quality charge transport properties, similar to their carbon predecessor^{4,5}. The hydrogenated form of germanene, known as germanane, has recently been synthesised for the first time by Bianco et al.⁶. The crystal structure of germanane consists of a hexagonal germanium lattice with hydrogen atoms (H) covalently bonded to every germanium atom (Ge) as shown in Figure 5.2-1 (a). Germanane is of particular interest, because in addition to high quality transport it is expected to have a band gap, similar to its graphene analogue graphane⁷⁻⁹. In Bianco et al.⁶ the band gap of the germanane was experimentally estimated from diffuse reflectance absorption spectroscopy to be around 1.59 eV, close to the calculated values reported⁷⁻⁹. Until now the number of available publications on this material is still very limited, covering theoretical investigation of the band structure⁷⁻¹¹ and very preliminary electrical characterisation¹²⁻¹⁴. The electron mobility, limited by electron-phonon scattering, was calculated to be around $20,000 \text{ cm}^2\text{V}^{-1}\text{s}^{-1}$ at room temperature⁶, which is strongly appealing for germanane to form a good basis for future application devices.

5.2 Device fabrication and characterization

To prepare the multilayer germanane flakes from powder we followed the protocol from Bianco et al.⁶, which involves the topochemical deintercalation of CaGe_2 . The precursor phase $\beta\text{-CaGe}_2$ was prepared by sealing a stoichiometric 1:2 ratio of calcium (granular Ca with purity 99% from Sigma-Aldrich) and germanium (Ge powder with purity 99.99%, Sigma-Aldrich) in a cylindrical alumina crucible (external diameter of 11 mm) enclosed in an evacuated fused quartz tube (internal diameter of 12 mm). The mixing of the two metals and the filling of the crucible was performed in a glove box under nitrogen atmosphere. The sealed quartz tube was then placed in a box furnace and the following temperature profile was employed: (1) heating to 1025°C within 2 hours at a rate of $8.3^\circ\text{C}/\text{min}$; (2) homogenization at 1025°C for 20 hours; (3) slow cooling to 500°C at a rate of $0.1^\circ\text{C}/\text{min}$ and finally (4) cooling further to room temperature at a rate of $0.2^\circ\text{C}/\text{min}$. Small crystals (2-6 mm) of CaGe_2 were collected and treated with an aqueous HCl solution 37% w/w (12 M) at -40°C under stirring for 7 days. The final product (GeH) was then separated by centrifugation, washed several times with distilled water (and finally methanol), and left to dry under vacuum. No trace of a calcium signal was detected in the measured energy-dispersive X-ray spectrum of our sample, confirming the successful topotactic deintercalation of $\beta\text{-CaGe}_2$ and the formation of germanane (GeH) product. The quality of our germanane powder has been confirmed by a set of characterisation techniques including X-ray diffraction, FTIR spectroscopy, Raman spectroscopy and DRA measurements (see section 5.5), which fully verify that the synthesised material is indeed germanane.

The prepared powder was further processed to fabricate transistors. Germanane flakes were mechanically cleaved down to thicknesses ranging from 15 nm up to 90 nm and placed on top of a 300 nm Si/SiO₂ substrate. Ti/Au contacts (5 nm/100 nm) were made via standard

PMMA-based e-beam lithography, as shown in the optical image of a typical device in Figure 5.2-1 (b). Solvent residue was evaporated from the resist film by baking at 150 °C for 90 sec. It was shown in^{6,15} that prolonged temperature treatment of germanane above 75 °C in 5% H₂/Ar can cause an amorphisation process. To exclude the possibility that brief heat treatment might cause a change in the crystal structure, we made a follow-up device (sample 2) without baking, which showed quantitatively the same behaviour as sample 1 (see section 5.5). Of four prepared devices, only two were found to be electrically connected by the electrodes, presumably due to the fast oxidation of the germanane surface. Both working devices were prepared within a relatively short time period of 12 hours between the exfoliation and contact deposition in order to minimise the oxidation effect. Thickness of the flake was determined by atomic force microscopy (AFM), shown in Figure 5.2-1 (c) and (d) to be 60 nm. All electrical measurements were performed in a DC current mode with the use of a Keithley 2410 source measure unit in both a vacuum chamber and a cryostat. The samples were stored and measured in vacuum with pressures of below 10⁻⁵ mbar in the sample space.

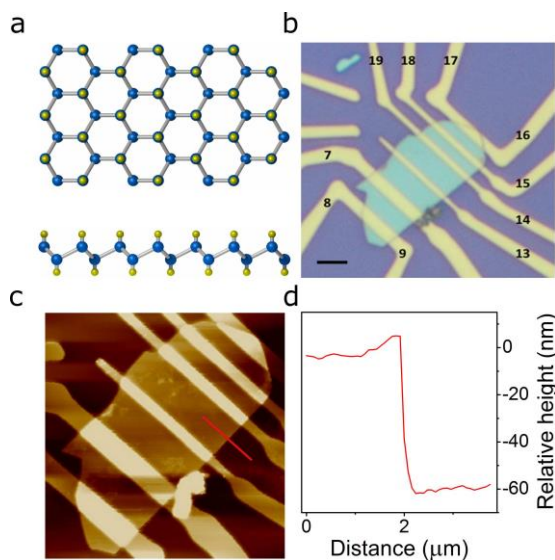


Figure 5.2-1 (a). Schematic representation of a germanane monolayer (top and side views) with Ge atoms (blue) at the corners of hexagons and H atoms (yellow) bonded to Ge. (b). Optical image of the germanane flake based device on top of a Si/SiO₂ substrate with Ti/Au electrodes (Scale bar is 3 μm). (c). AFM image of the germanane transistor. (d). The height profile is plotted along the red line as shown in panel (c) giving the flake thickness to be 60 nm.

5.3 Measurement

As initial electrical characterization we performed resistance measurements at room temperature in the linear regime (the measured voltage scales linearly with the applied current). We measured the voltage V in a 2-terminal configuration when a constant current of 2 nA was supplied, shown as the blue curve in Figure 5.3-1 (a). The signal was measured as a function of the applied gate voltage V_G , revealing a peak-like feature. The appearance of this maximum is associated with tuning of the Fermi level of the material in the band gap, implying that the studied device is ambipolar or, in other words, indicating the possibility to

electrically dope it with both holes and electrons. It is worth noting here that the position of the maximum close to $V_G=0$ V indicates a relatively low intrinsic doping of the material.

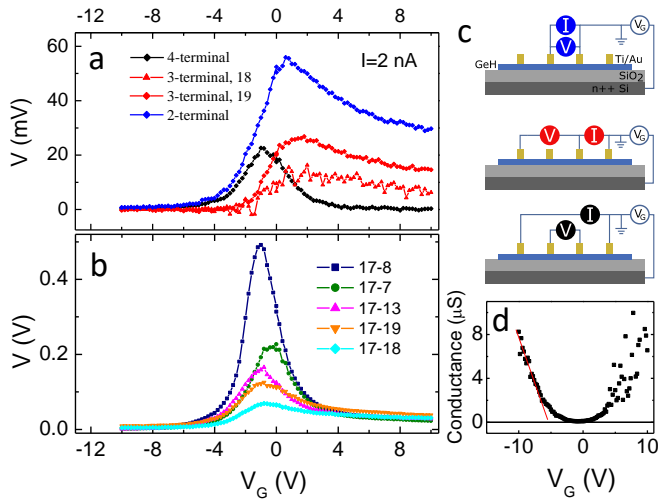


Figure 5.3-1 (a). Measured signal V plotted for 2-terminal (blue), 3-terminal (red) and 4-terminal (black) configurations as a function of the gate voltage. The 3-terminal measurements were performed using both contacts 18 (triangles) and 19 (diamonds). The applied constant current between source and drain was 2 nA, and the measurements were performed at room temperature. (b). 2-terminal measurements as a function of V_G performed using different distances between the contacts while keeping the same source contact. The resistance values at the curve maxima scale approximately with the channel length (for the sample geometry, see Figure 5.2-1 (b)). $I = 2$ nA. (c). 2-, 3- and 4-terminal measurement configurations allow the contact and channel-related resistances to be extracted separately. (d). Room temperature conductance calculated from the 4-terminal measurement shown in panel (a); the red line represents a linear fit resulting in a mobility of $30 \text{ cm}^2\text{V}^{-1}\text{s}^{-1}$.

A semiconductor, when brought into direct contact with a metal, forms a Schottky barrier which usually results in a relatively high contact resistance and thus affects the measured 2-terminal $V(V_G)$ dependence. To circumvent the influence of the resistive contacts and distinguish between channel and contact properties, 4-terminal electrode configurations were used. In Figure 5.3-1 (a) different multiterminal measurements (see Figure 5.3-1 (c) for schematics of configurations) are shown together for a clear comparison. The 2-terminal measurement contains contributions from both the channel resistance and the two interface resistances (see section 5.5 for the resistance model used) and is seen to be asymmetric with respect to the peak position. In contrast, the 4-terminal voltage shows a much more symmetric dependence on V_G , as one would expect for a semiconducting material with similar electron and hole transport properties. The difference between the 2-terminal and 4-terminal curves is ascribed to the contact resistances and can be probed more directly in a 3-terminal configuration. The measured dependencies indeed indicate that the observed asymmetry is related to the transport through or in the vicinity of the contact interface and can be explained by the presence of the expected Schottky barriers at each contact interface. The degree and sign of the asymmetry (as for the height and position of the Schottky barrier itself) are determined both by the Fermi level positions in the adjacent regions and by the properties of the interface such as the density of impurity states. We note that in addition to formation of

the Schottky barrier, the metal contact can also lead to modification of the underlying bulk channel. In this scenario the contact contribution cannot be excluded even in a 4-terminal configuration (see section 5.5 for more details).

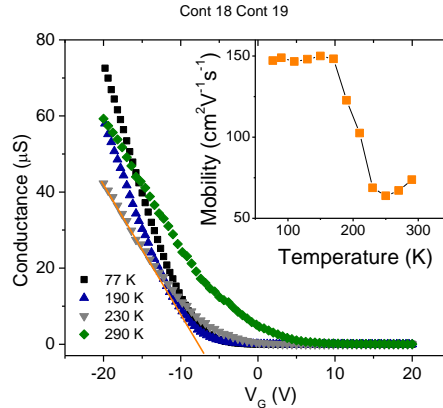


Figure 5.3-2 The 2-terminal conductance for contacts 18 and 19 is plotted as a function of V_G at different temperatures. The orange line represents an example of a linear fit for the extraction of hole mobility. The perceived 2-terminal hole mobility is expected to be close to the actual channel mobility because (as shown in Figure 5.3-1) the contact contribution at negative gate voltages is minimal. The gate voltage was swept from positive to negative values. Inset: 2-terminal hole mobility extracted from the data plotted in the main panel, shown as a function of temperature.

An alternative way to differentiate between the channel and contact properties is to measure 2-terminal resistances for different channel lengths. In Figure 5.3-1 (b) we plot 2-terminal resistances measured with source contact 17 while the drain contact was varied over all possible configurations (see Figure 5.3-1 (b)). The central portion of the curves around the maxima scales approximately with the channel length L , while for large positive gate voltages the measured signals saturate at values that are independent of L . This further confirms a clear distinction between the channel associated resistance and the asymmetric contribution attributed to the contact regions, which influences the measurement mostly at positive V_G .

In order to explore the higher carrier concentration regime, we extended the range of used gate voltages up to ± 50 V. At the maximum V_G range, an ON-OFF current ratios for the holes is found to be 10^4 at room temperature and 10^5 at 77 K (see section 5.5). At $|V_G| > 10$ V a prominent hysteretic behaviour develops that is most pronounced at higher temperatures where the difference between the positions of the minima for opposite sweeping directions can be as large as ~ 60 V for a sweeping range of ± 50 V (at sweeping rate of ~ 0.1 V/s). Such hysteresis indicates the presence of a substantial number of charge trap states within the range over which the Fermi level varies. Under an applied gate voltage these traps become activated/deactivated and can modulate the effective doping level of the system, thus affecting the shape of the conductivity dependence. At lower temperatures charge traps become frozen, considerably diminishing the degree of hysteresis and improving the reliability of the mobility estimation. For clarity, in our subsequent analysis below we use measurements performed with the same sweep direction from positive to negative V_G unless stated otherwise (Figure 5.3-2). The mobility is estimated from the linear high carrier

concentration part of the conductance dependence as a function of V_G and is plotted as a function of temperature in the inset. The observed increase in mobility with decreasing temperature could suggest a significant reduction of the contribution of the phonon scattering to the transport properties of carriers. Alternatively such temperature dependence of the extracted mobility can be artificially induced by the temperature dependent hysteretic behaviour of the measured conductance. However, such mobility extraction is still reliable at low temperatures where the observed hysteresis is minimal. Below about 170 K, the mobility saturates at $\sim 150 \text{ cm}^2/\text{Vs}$. This exceeds the value estimated from the room temperature, low V_G range dependence (Figure 5.3-1 (d)), presumably due to the fact that in the low V_G range the system does not yet reach the linear conductivity regime as the Fermi level is still in the transition from the band gap to the valence band. Furthermore, electron transport is observed to be significantly suppressed compared to hole transport due to the presence of both hysteresis and the contact contribution in the 2-terminal measurement configuration as discussed earlier. Therefore, the set of performed measurements does not allow us to characterize the temperature dependence of the electron transport.

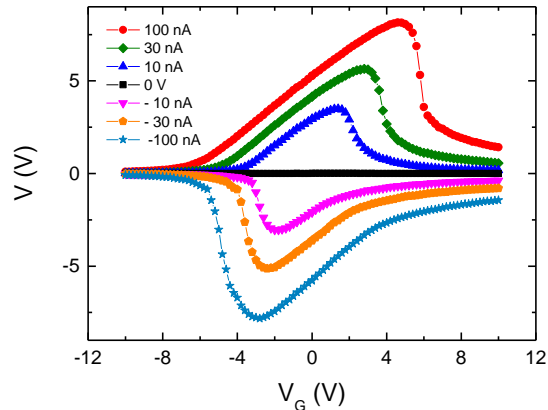


Figure 5.3-3 Room temperature 4-terminal voltage measured as a function of V_G for a set of different bias currents at room temperature. The current was applied between contacts 17 and 7, while the voltage was measured between contacts 19 and 13.

To further demonstrate the transistor action of germanane in the non-linear regime, we repeated the 4-terminal voltage measurements using applied currents up to 100 nA, as shown in Figure 5.3-3. In this regime the voltage drop along the channel becomes comparable with the applied gate voltage and therefore creates an easily observable additional doping effect that changes along the length of the transport channel. These transport measurements probe an effect that can be approximated to first order by an average doping value, i.e., an extra gating of $V/2$. This means that under an applied voltage V across the channel, the measured dependencies are expected to be shifted by $V/2$. Such a shift is indeed seen in Figure 5.3-3. For instance, when the applied bias current is 100 nA the voltage across the sample at the maximum is ~ 8 V. The position of the maximum is shifted with respect to its linear regime position (see Figure 5.3-1 (a)) by ~ 5 V, which is close to the expected $8/2$ V. The small degree of asymmetry between positive and negative applied currents indicates intrinsic asymmetry in the device and is further discussed in the section 5.5.

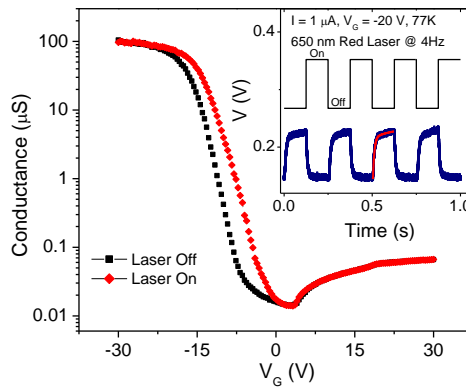


Figure 5.3-4 4-terminal conductance shown as a function of the gate voltage measured in the dark (black squares) and under red laser illumination (red diamonds). The current was applied between contacts 17 and 8, while the voltage was measured between contacts 18 and 19. $I=1 \mu\text{A}$, $T=77 \text{ K}$. Inset: 4-terminal V plotted as a function of time when the laser is switched ON and OFF with chopper at 4 Hz. Applied $V_G=-20 \text{ V}$, $I=1 \mu\text{A}$. The red curve represents a fit using a double exponential dependence resulting in two characteristic times, 8.3 ms and 0.20 s. The black line shows the laser intensity, plotted in arbitrary units, which was switched between 0 and $\sim 40 \text{ mW/cm}^2$.

So far we have presented measurements performed in the dark, thus avoiding influence of ambient light on the transport characteristics of germanane. However, the theoretical studies⁷⁻⁹ suggest the presence of a direct band gap in germanane, which implies a substantial response of the material to light excitation of the appropriate wavelength. Accordingly, we performed an experiment where the channel conductance in 4-terminal configuration was measured both in the dark and under illumination, shown in Figure 5.3-4. For the light source we used a red laser with a wavelength of 650 nm and an intensity of $\sim 40 \text{ mW/cm}^2$. The increase of the conductance under illumination over a certain gate voltage range (swept from negative to positive values) can suggest the excitation of extra carriers by photons as it happens in direct band gap materials. However, the substantial hysteresis in the system that is also observed indicates the presence of charge traps in the channel or in its vicinity. Such trap states can also be optically active and can influence the response to the illumination. The time responses of a trap system and a band electron system are expected to be significantly different because band electron systems reach equilibrium relatively fast compared to trap states. In the inset to Figure 5.3-4 we show the electrical response measured in 4-terminal configuration as a function of time when the laser light was modulated with a chopper at a frequency of 4 Hz. Double exponential fitting clearly indicates two components with characteristic times of $t_1 \approx 0.20 \text{ s}$ and $t_2 \approx 8.3 \text{ ms}$. Since the trap-associated processes are expected to be much longer than those associated with band carriers, we interpret the appearance of a long time t_1 as an indication of trap states in the vicinity of the channel. The short time t_2 is consistent with the bandwidth limitation of our electrical measurement circuit (RC time limitation), which masks the real time scale of the fast response. The time response of band electrons in similar systems is typically faster than 1 ns (for GaAs see¹⁶). Therefore, further investigation with a higher frequency bandwidth is needed in order to characterize the photo response of the device at short timescales.

5.4 Conclusion

In conclusion, in this work we have demonstrated the realization of single crystal germanane field-effect transistors with a current ON-OFF ratio in the range of 10^4 - 10^5 , depending on the temperature. By employing various multiterminal measurement configurations, we have clearly separated the transport properties of the germanane channel from those of the contacts. Low gate voltage dependence measured at room temperature clearly reveals that germanane exhibits ambipolar behaviour. We have found a low bound for the hole mobility to be $70 \text{ cm}^2/\text{Vs}$ at room temperature which further increases to $\sim 150 \text{ cm}^2/\text{Vs}$ below 150 K. Moreover, our study of the influence of light illumination confirms the high responsivity of the material, although further investigations are needed to fully characterize the photo response.

5.5 Supplementary information

5.5.1 X-ray diffraction

Single-crystal X-ray diffraction (XRD) measurements were performed using a Bruker D8 Venture diffractometer operating with Mo $K\alpha$ radiation and equipped with a Triumph monochromator and a Photon100 area detector. The crystals were mounted on a 0.3 mm nylon loop using cryo-oil. An Oxford Cryosystems Cryostream Plus was used to cool the samples to 100 K for data collection using a nitrogen flow. Data processing was performed using the Bruker Apex II software; the structure was solved by direct methods and refined using the SHELXL software¹⁷. Powder XRD data were collected using a Bruker D8 Advance diffractometer operating in Bragg-Brentano geometry with Cu $K\alpha$ radiation. The data were fitted using the GSAS software suite¹⁸.

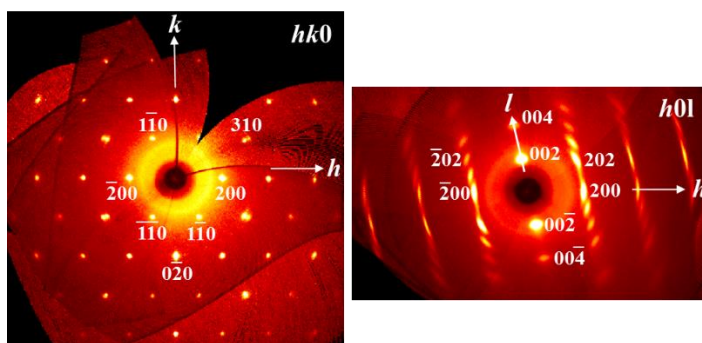


Figure 5.5-1 $hk0$ and $h0l$ reciprocal lattice images reconstructed from raw single-crystal XRD data.

The sample contained many small, dark brown crystals. A rectangular block-like crystal of dimensions $0.1 \times 0.05 \times 0.02$ mm was chosen for structure determination by single-crystal XRD. The unit cell was found to be monoclinic with lattice parameters $a = 6.9244(14)$ Å, $b = 3.9978(14)$ Å, $c = 10.939(5)$ Å, $\beta = 102.181(1)^\circ$. Inspection of reconstructed reciprocal lattice sections (Figure 5.5-1) showed that the condition $h+k=2n$ is obeyed, implying a C-centered lattice. Intensity statistics suggested a non-centrosymmetric structure, thus structure solution and refinement were attempted in space groups $C2$ and Cm . The Ge framework structure was solved by direct methods using the intensities of 373 unique reflections and the best solution (in terms of goodness of fit and residual electron density) was obtained using $C2$. Hydrogen atoms were added using the “riding” model incorporated in SHELXL, assuming tetrahedral coordination of Ge and fixed Ge-H bond distances of 1.565 Å¹⁹. A view of the refined structure is shown in Figure 5.5-2 and the atomic parameters are listed in Table 5.5-1.

In Figure 5.5-1 it is apparent that the pseudo-hexagonal $hk0$ -plane (left) is well defined, containing sharp spots, whereas the spots along the l -direction (right) exhibit streaking, indicating short range order in the layer stacking direction. This is consistent with a previous report on germanane⁶. Nevertheless, the $00l$ spots are well distinguished, allowing the

average stacking periodicity to be established.

Atom	Ge1	Ge2	H1	H2
x	0.6557(8)	0.6784(18)	0.6069	0.7267
y	0.3589(16)	0.9306(16)	0.3589	0.9306
z	0.9678(9)	0.5386(14)	0.8214	0.685
U_{11} (\AA^2)	0.012(3)	0.092(8)	0.067	0.123
U_{22} (\AA^2)	0.029(4)	0.018(4)		
U_{33} (\AA^2)	0.131(8)	0.202(13)		
U_{12} (\AA^2)	-0.001(4)	0.005(4)		
U_{13} (\AA^2)	0.029(3)	0.041(8)		
U_{23} (\AA^2)	0.005(4)	-0.003(4)		

Table 5.5-1 Refined atomic coordinates and displacement factors for germanane at 100 K. Hydrogen positions were generated automatically by geometrical considerations. Space group C2: $a = 6.9244(14)$ \AA , $b = 3.9978(14)$ \AA , $c = 10.939(5)$ \AA , $\beta = 102.181(1)^\circ$.

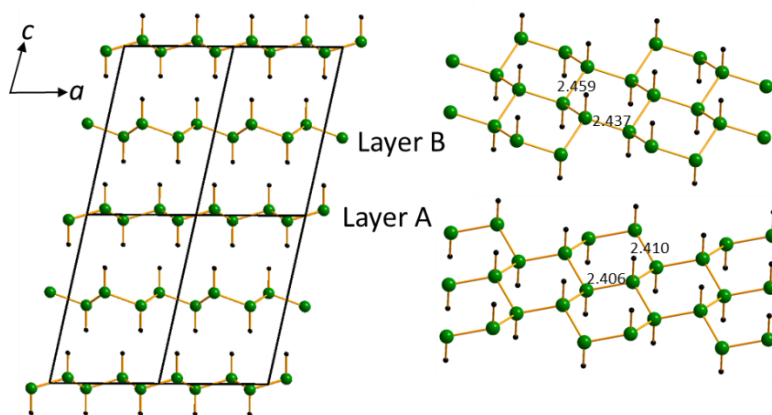


Figure 5.5-2 Refined crystal structure from single-crystal XRD data. The 6-membered Ge rings adopt the “chair” configuration. Views of layers A and B (right) show the crystallographically distinct Ge-Ge bond distances (Ångstrom).

In the refined structure in Figure 5.5-2 it can be seen that the Ge atoms form 6-membered rings in the “chair” configuration. There are two crystallographically independent layers which are stacked in an ABAB sequence along the c-axis. The lateral offset between successive layers gives rise to a monoclinic unit cell. The seventh layer is almost directly

above the first layer; this would correspond to the 6-layer rhombohedral unit cell of β -CaGe₂ (space group R-3m) with which Luo and Zurek¹⁹ argued that germanane should be isostructural. The transformation from the rhombohedral to monoclinic cell is given by the matrix [1, -1, 0; 1, 1, 0; -1/3, 1/3, 1/3]. Indeed, our single-crystal XRD data could be indexed assuming a rhombohedral cell with $a = 3.998 \text{ \AA}$, $c = 32.078 \text{ \AA}$. We thus carried out structure solutions and refinements in the space groups R-3m, R3m and R3. The best fit was obtained in R3m but with an RF^2 factor slightly larger than the C2 solution (0.187 versus 0.177) and with a significantly larger residual electron density. We therefore conclude that the structure is very close to that of β -CaGe₂, but with a slight monoclinic distortion. We note that the RF^2 fit factors are relatively high due to the diffuse scattering associated with stacking disorder (Figure 5.5-1).

The disorder in the stacking direction can also be seen in powder XRD patterns collected at room temperature and above on part of the bulk sample that was finely ground (Figure 5.5-3). The intense 002 peak is extremely broad. The width of this peak allows a rough estimate of the correlation length; use of the Scherrer formula gives an estimate of $\sim 50 \text{ \AA}$ (~ 5 unit cells) in the c -direction. The strongly anisotropic peak broadening gives rise to problems in fitting the powder XRD pattern well, but the fit is rather good assuming the C2 structure obtained from the single crystal XRD data. There is a small amount of α -Ge in the sample: the ratio of GeH to α -Ge is 94(2)% to 6(2)%.

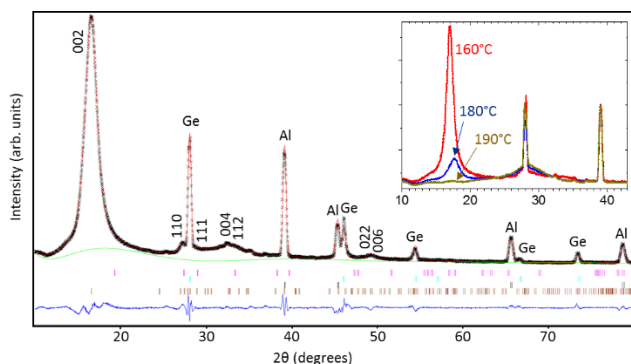


Figure 5.5-3 Observed (black data points), calculated (red line) and difference (blue line) powder XRD profiles at 40 °C. The Al peaks are from the sample holder. The inset shows the disappearance of the 002 peak as the sample is heated from 160 °C to 190 °C.

On heating, no changes are observed in the powder XRD patterns up to 160 °C apart from slight peak shifts due to thermal expansion. The GeH peaks decrease strongly in intensity at 180 °C and have disappeared at 190 °C (inset to Figure 5.5-3). On cooling again the peaks do not reappear, implying that there is an irreversible crystalline to amorphous transition on heating.

Therefore, with XRD spectroscopy we unambiguously determine the crystallographic structure of the synthesised material to be identical to that of GeH.

5.5.2 FTIR spectroscopy

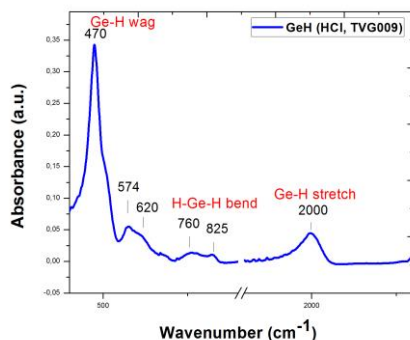


Figure 5.5-4 FTIR spectrum of GeH

Fourier transform infrared spectra were measured in the range of 400–4000 cm^{-1} with a Shimadzu FTIR 8400 spectrometer equipped with a deuterated triglycine sulfate (DTGS) detector. Each spectrum was the average of 32 scans collected with 2 cm^{-1} resolution. Samples were in the form of KBr pellets containing ca. 2 wt % of sample. The spectrum of germanane shows a strong peak at 2000 cm^{-1} due to Ge-H stretching vibration while peaks at 470, 574 and 620 cm^{-1} assigned to multiple wagging modes of Ge-H^{6,20}. Moreover, weak peaks at 760 and 825 cm^{-1} are also present which correspond to H-Ge-H bending modes from neighbouring Ge atoms at the edges of the crystalline germanane layer and/or Ge vacancies within the layered germanane lattice⁶. Based on the FTIR spectroscopy we confirmed hydrogen termination of germanium atoms in the synthesised germanane (GeH).

5.5.3 UV-Vis-NIR/DRA measurements

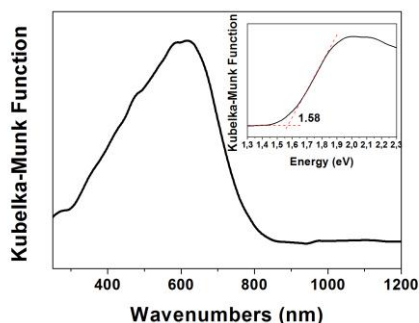


Figure 5.5-5 DRA spectrum of GeH plotted in Kubelka-Munk function versus wavenumbers/ photon energy

The diffuse reflectance measurements were conducted using a Shimadzu UV-VIS-NIR

Spectrophotometer (UV-3600) equipped with an integrating sphere attachment on barium sulfate coatings. The diffuse reflectance spectrum was converted to Kubelka-Munk function, $F(R_\infty)^{6,21}$ and plotted against wavenumbers (nm) and photon energy (eV). The line tangent to the point of inflection on the curve and the eV value, at the point of intersection of the tangent line determined E_g value close to 1.58 eV. Thus, with DRA spectroscopy we confirm the presence of a band gap with the value which is very similar to that reported for germanane⁶.

5.5.4 Raman spectroscopy

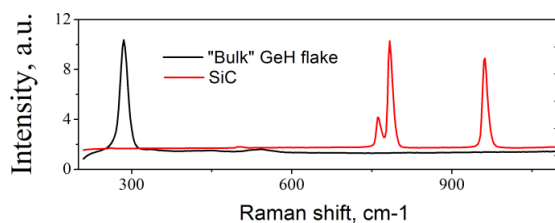


Figure 5.5-6 Raman spectrum of bulk germanane powder flake (black) transferred on top of a SiC substrate, where SiC spectrum (red) shown separately. A characteristic peak associated with Ge-H bond is seen at 285 cm^{-1} .

Raman spectra were collected using a 632.8 nm excitation laser with a spot size of $2\text{ }\mu\text{m}$ using an Olympus BX51 microscope coupled to a HeNe Laser (10 mW, Thorlabs) and a Shamrock 163 spectrograph and iDus-420-OE CCD (Andor Technology). The Raman spectrum of the synthesized powder flake clearly reveals the presence of the Ge-H bond in the studied material thus confirming its composition.

5.5.5 Resistance model for 4-terminal measurement

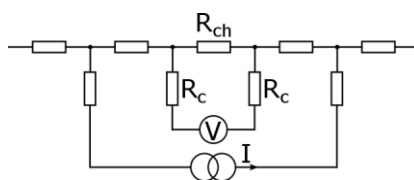


Figure 5.5-7 Schematics of the used resistance network model for multiterminal measurements. Horizontal resistances R_{ch} line represent the channel divided into sections between the contacts which are shown with vertical resistances R_c .

For interpretation of the 3- and 4-terminal measurements we employ a standard resistance network model shown in Figure 5.5-7. Within such a model the contact contribution R_c is fully excluded when 4-terminal configurations is used. 3-terminal measurement unambiguously gives the contact resistance R_c . However, in reality the metal contact locally modifies the semiconductor channel underneath it, forming, for example, p-n junctions in the channel or depletion regions. This implies that $R_{ch}=r_{ch}+r_{ch}^*$, where r_{ch} is true unaffected channel resistance and r_{ch}^* is the part of the channel modified due to the contact. Under these circumstances even a 4-terminal configuration contains not only the intrinsic channel

resistance but also contact induced contribution.

5.5.6 Non-linear I-V characteristics

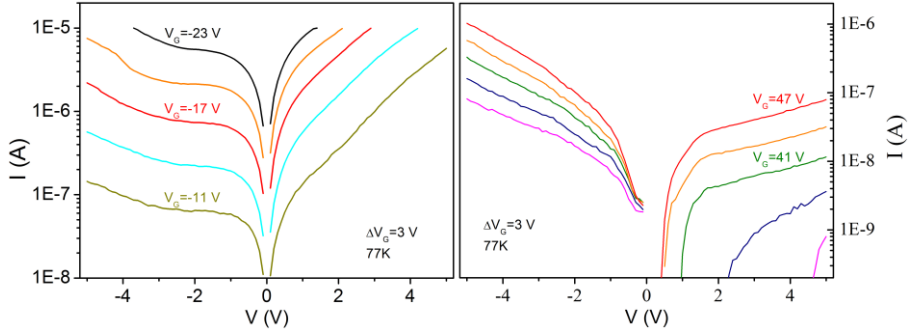


Figure 5.5-8 2-terminal I-V characteristics of the device measured between contacts 18 and 19 and plotted in logarithmic scale with respect to the source-drain bias for different gate voltages for both hole doped (left) and electron doped (right) regimes. For $V < 0$ V the value of the current is multiplied with -1 for the applicability of the logarithmic scale.

We measured I-V characteristics of the device in 2-terminal configuration for different gate voltages, Fig S8. Overall the measured output curves resemble transistor-like behaviour. In particular, for $V < 0$ in a certain ranges of the gate voltage we observed consistently a current saturation regime that is followed by a breakdown regime where the source-drain current transits into an exponential increase. However, at $V > 0$ a saturation regime is practically absent implying that the output curves are highly asymmetric with respect to $V = 0$. Assuming a homogeneous channel the strong asymmetry in I-V characteristics unambiguously suggests an asymmetry between the Schottky barriers formed at source and drain contacts. This is not immediately expected as both of the contacts used for measurements are geometrically designed to be the same (contact 18 and 19 in Figure 5.2-1, main text) and there is no step in our fabrication procedure that would make a clear distinction between them. Nevertheless, experimentally the 3-terminal dependences $V(V_G)$ for these contacts indeed reveal substantial difference in their resistances as seen in Figure 5.3-1, main text. With a certain extension this situation is similar to a p⁺np bipolar transistor with similar asymmetric I-V characteristics.

5.5.7 Four-terminal transfer curves at higher gate voltage range

Higher gate voltages up to ± 50 V (at 0.1 V/s sweep rate) were probed to achieve higher charge carrier concentration. In Figure 5.5-9 conductance is plotted within a maximum used gate voltage range in semilogarithmic scale both at room temperature and 77 K. The observed modulation of the conductance with applied V_G gives an ON-OFF current ratio $\sim 10^4$ at room temperature and $\sim 10^5$ at 77 K. As mentioned in the main text a significant hysteresis develops when V_G is swept in a range larger than ± 10 V. For a given range of ± 50 V the difference in conductance minima positions in opposite sweeping directions is found to be as large as ~ 60 V at room temperature. Presence of such hysteresis is likely to be due to the existence of charge

trap states.

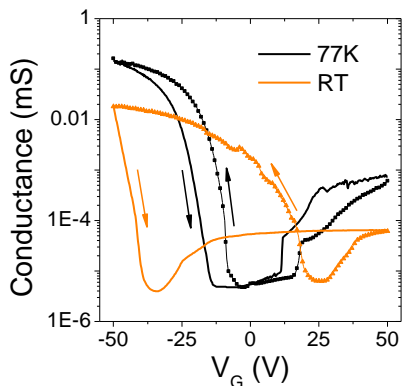


Figure 5.5-9 4-terminal conductance plotted in a semilogarithmic scale as function of V_G for both room temperature (orange) and 77K (black). The current was applied between contacts 17 and 8, while the voltage was measured between contacts 19 and 13. Arrows indicate the direction of the sweeping gate voltage.

5.5.8 Electrical characterization of sample #2

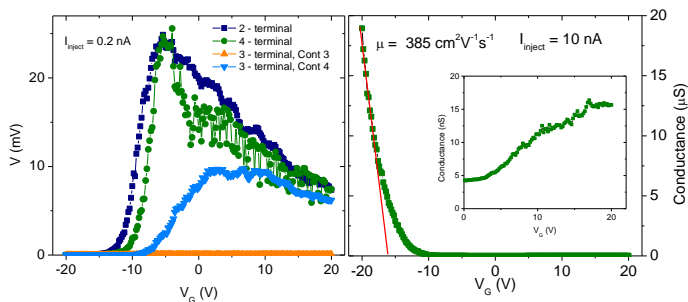


Figure 5.5-10 Left: measured signal V for sample #2 is plotted for 2-terminal (blue), 3-terminal (red) and 4-terminal (black) configurations as a function of the gate voltage. 3-terminal measurements are done for contacts 3 and 4. The applied constant current between source and drain is 0.2 nA, measurements are done at room temperature. Right: 4-terminal conductivity V/I measured at room temperature as function of V_G . The red line represents a linear fit and gives $\sim 400 \text{ cm}^2/(\text{Vs})$ for the hole mobility. The gate voltage is swept from negative to positive values. The inset shows a zoomed in region for positive gate voltage range of the dependence from the main panel.

One of the consequences of the formed Schottky barrier at the interface is a doped (depleted) region in the vicinity of the contact. The affected region spreads out as far as the depletion width (both in plane of the flake and beneath the contact) and can generally contribute to the electrical transport as an extra resistance. Depending on the thickness of the studied semiconductor with respect to the depletion width such regions/junctions will affect the 4-terminal measurements to a different extent. As compared to sample #1 discussed in the main text (see Figure 5.3-1) it is seen that contact contribution for sample #2 is much more pronounced even in a 4-terminal configuration. It suggests a significant modification of the channel under the contact. Moreover, it is apparent that for sample #2 2-terminal

measurement cannot be obtained by summing up both 3-terminals and 4-terminal measurements. For this sample the leakage current between the Si gate and the germanane flake was found to be relatively high compared to sample #1 and reached up to 3 nA which is comparable to the applied current and, therefore, is likely to influence the measured voltage in all configuration. Leakage current for sample #1 was found to be below the noise level of the measurement (typically ~ 1 nA) at all gate voltages.

Besides the leakage sample #2 showed a qualitatively similar behaviour to the sample discussed in the main text, including the value for the hole mobility ~ 400 cm²/(Vs) estimated from 4-terminal measurements at 77 K.

References

1. Butler, S. Z. et al. Progress, challenges, and opportunities in two-dimensional materials beyond graphene. *ACS Nano* **7**, 2898–2926 (2013).
2. Geim, A. K. & Grigorieva, I. V. Van der Waals heterostructures. *Nature* **499**, 419–425 (2013).
3. Li, S.-L., Tsukagoshi, K., Orgiu, E. & Samorì, P. Charge transport and mobility engineering in two-dimensional transition metal chalcogenide semiconductors. *Chem. Soc. Rev.* **45**, 118–151 (2016).
4. Balendhran, S., Walia, S., Nili, H., Sriram, S. & Bhaskaran, M. Elemental Analogues of Graphene: Silicene, Germanene, Stanene, and Phosphorene. *Small* **11**, 640–652 (2014).
5. Wang, M., Liu, L., Liu, C.-C. & Yao, Y. van der Waals heterostructures of germanene, stanene, and silicene with hexagonal boron nitride and their topological domain walls. *Phys. Rev. B* **93**, 155412 (2016).
6. Bianco, E. et al. Stability and Exfoliation of Germanane: A Germanium Graphane Analogue. *ACS Nano* **7**, 4414–4421 (2013).
7. Houssa, M. et al. Electronic properties of hydrogenated silicene and germanene. *Appl. Phys. Lett.* **98**, 223107 (2011).
8. Lew Yan Voon, L. C., Sandberg, E., Aga, R. S. & Farajian, A. A. Hydrogen compounds of group-IV nanosheets. *Appl. Phys. Lett.* **97**, 163114 (2010).
9. Shu, H., Li, Y., Wang, S. & Wang, J. Thickness-Dependent Electronic and Optical Properties of Bernal-Stacked Few-Layer Germanane. *J. Phys. Chem. C* **119**, 15526–15531 (2015).
10. Qi, J., Li, X. & Qian, X. Electrically controlled band gap and topological phase transition in two-dimensional multilayer germanane. *Appl. Phys. Lett.* **108**, 253107 (2016).
11. Zólyomi, V., Wallbank, J. R. & Fal'ko, V. I. Silicene and germanene: tight-binding and first-principles studies. *2D Mater.* **1**, 11005 (2014).
12. Amamou, W. et al. Large area epitaxial germanane for electronic devices. *2D Mater.* **2**, 35012 (2015).
13. Young, J. R. et al. Water activated doping and transport in multilayered germanane crystals. *J. Phys. Condens. Matter* **28**, 34001 (2016).
14. Sahoo, N. G. et al. Schottky diodes from 2D germanane. *Appl. Phys. Lett.* **109**, 23507 (2016).
15. Jiang, S., Bianco, E. & Goldberger, J. E. The structure and amorphization of germanane. *J. Mater. Chem. C* **2**, 3185–3188 (2014).
16. M. R. Brozel, G. E. S. Properties of Gallium Arsenide. (INSPEC, 1996).
17. Sheldrick, G. M. A short history of SHELX. *Acta Crystallogr. Sect. A* **64**, 112–122 (2008).
18. Larson, A. C. & Dreele, R. B. General Structure Analyst System. Los Alamos Natl. Lab. Rep. **86–748**, (2004).
19. Luo, X. & Zurek, E. Crystal Structures and Electronic Properties of Single-Layer, Few-Layer, and Multilayer GeH. *J. Phys. Chem. C* **120**, 793–800 (2016).

-
20. Jiang, S. et al. Improving the stability and optical properties of germanane via one-step covalent methyl-termination. *Nat. Commun.* **5**, 3389 (2014).
 21. Liu, Z. et al. GeH: A novel material as a visible-light driven photocatalyst for hydrogen evolution. *Chem. Commun.* **50**, 11046–11048 (2014).